An RPA-LDA treatment of density fluctuations in the alkali metals Na and Cs

1995 J. Phys.: Condens. Matter 7 3153

(http://iopscience.iop.org/0953-8984/7/16/010)

J. Phys.: Condens. Matter 7 (1995) 3153–3171. Printed in the UK

An RPA–LDA treatment of density fluctuations in the alkali metals Na and Cs

M Kollwitz and H Winter

Kernforschungszentrum Karlsruhe, Institut für Nukleare Festkörperphysik, PO Box 3640, D-76128 Karlsruhe, Germany

Received 20 October 1994, in final form 13 January 1995

Abstract. We calculate the density fluctuation spectra of the alkali metals Na and Cs in the RPA approximation, using KKR band structure data. The Coulomb part of the **K** matrix is augmented by a local exchange and correlation term derived from the LDA. In the case of Na we find well defined plasmon excitations in the wave vector range below $q_c \simeq 0.5$ (du) whose positions and widths are in reasonable agreement with experiment. In accordance with the features of its band structure the density response of Cs is more complicated. Nevertheless we find low-frequency peaks whose positions and widths could be interpreted as plasmon-like excitations.

1. Introduction

The frequency- and wave-vector-dependent density correlation function of a metal is an important quantity, influencing various equilibrium and non-equilibrium properties. Theoretical results may be directly compared to experiment, because electron energy loss spectroscopy (EELS) measures the imaginary part of the real space double Fourier transform of this function, called the density fluctuation spectrum in the following.

Its theoretical treatment is an intricate many-body problem involving substantial approximations for the single-particle propagator and the electron–hole irreducible **K** matrix entering the Bethe–Salpeter equation. In the absence of any analogon to the Migdal theorem of phonon theory or a small parameter suggesting some kind of perturbational approach, it is hard to give an *a priori* justification of any approximation used in applications to realistic systems. We lay, however, stress on treating the problem from first principles, avoiding the introduction of parameters and taking account of the lattice structure of the system in question.

As a first approach an RPA-like treatment, based on KKR band structure, seems reasonable to us. From local density functional theory (LDA) we derive a **K** matrix consisting of the sum of the Hartree term and a local exchange–correlation part. This approximation may be shown to be charge conserving.

In a recent application to the transition metal V for the case of small wave vectors (Winter 1993 and references therein) we have demonstrated that this kind of approximation can describe significant features revealed by EELS experiments: even in the wave vector regime where continuum theories would predict weakly damped plasmons, the fluctuation spectrum as obtained by RPA–LDA exhibits a broad distribution with its maximum position at 21 eV, in agreement with experiment. Theory shows that this behaviour is caused by the presence of the crystalline lattice and the strong deviation of the Bloch states from plane waves. In order to achieve a still more detailed agreement, especially in the low-frequency

0953-8984/95/163153+19$19.50

regime, the evaluation of the polarization function beyond the electron–hole bubble diagram would be required.

In the case of the alkali metals the principal questions are as follows. What is the wave vector range of plasmon-like excitations? Is the RPA–LDA able to describe their positions and widths reasonably, though, at variance with the transition metals, we are dealing here with systems of low electronic density? Is there any substantial difference between the behaviour of the light and the heavier alkali metals?

There have been important developments during the last few years in the theory of the density response of the alkali metals. Quong and Eguiluz (1993) present a first-principles method in the frame of the RPA and the TDLDA amounting to including the derivative of the exchange and correlation potential in the kernel of the Bethe–Salpeter equation. Using a scheme that avoids direct summation over unoccupied bands and employing a plane wave basis set they evaluate the density response of Na and Al. Aryasetiawan and Karlsson (1994) evaluate the energy loss spectra of the alkali metals within the RPA using a band structure method derived from the LMTO. In their calculations they replace the δ function in the imaginary part of the dielectric function by a Gaussian. Zaremba and Sturm (1991) calculated the non-local dielectric function of the alkali metals in the region of the p core excitation threshold.

In spite of the fact that our present work is similar to that of Aryasetiawan and Karlsson (1994) we find it worthwhile to discuss it here, because our results have been independently obtained using a different band structure method. Some differences in the results show the great sensitivity of the theoretical density fluctuation spectra on the details of their evaluation.

In the following we concentrate on Na and Cs. An account of these results has already been given (Kollwitz and Winter 1994). This paper is organized as follows. In section 2 we discuss our KKR band structure results. In section 3 we show some relations visualizing the connection between band structure and density response. Section 4 is devoted to the presentation of the RPA–LDA dielectric functions and in section 5 we discuss our results for the density fluctuation spectra. We close with a summary in section 6.

2. The band structures of Na and Cs

We performed self-consistent scalar relativistic KKR band structure calculations for BCC Na and Cs using the lattice constants 4.225 Å and 6.045 Å, respectively, and for the exchange–correlation potential the expression derived by Hedin and Lundqvist (1971). The energy ranges (2.5 Ryd for Na and 1.2 Ryd for Cs) contain 20 energy eigenvalues. For their application to the density correlation function they have been evaluated on a mesh of 5000 $\boldsymbol{k}$ points in the irreducible wedge of the Brillouin zone (BZ). The Bloch state coefficients have been determined for angular momenta up to $l = 5$ and the formula of Ham and Segall (1961) has been worked out numerically to gain the Bloch wave functions on a dense mesh of points in the interstitial region of the unit cell. The single-particle states constructed in this way are sufficiently continuous across the muffin tin sphere radius and fulfil the boundary conditions on the surface of the unit cell to guarantee the mutual orthogonality of different wave functions within 1% accuracy. This degree of quality of the eigenstates is a necessary requirement for the realistic evaluation of the matrix elements entering the theory of the density response.

The fundamental differences between the band structures of Na and Cs may best be seen by comparing their density of states (DOS) curves (figure 1 and figure 2 for Na and Cs,

respectively.) At low energies they start with a parabolic shape due to the existence of the lowest occupied valence band. Their deviations from free-electron-like behaviour, especially near the BZ boundary, is clearly visible through humps in the DOS curves. Whereas the Fermi energy of Na ($\varepsilon_F = 0.231$ Ryd) falls into the free-electron regime, giving rise to a fairly spherical Fermi surface, substantial deviations from the free-particle behaviour are effective on the Fermi level of Cs ($\varepsilon_F = 0.1388$ Ryd) whose Fermi surface is markedly anisotropic. For Na we obtain $n(\varepsilon_F) = 6.49$ states Ryd^{-1}/atom and the values of the partial DOS are $n_0(\varepsilon_F) = 2.55$, $n_1(\varepsilon_F) = 3.29$, $n_2(\varepsilon_F) = 0.60$ and $n_3(\varepsilon_F) = 0.05$. The corresponding numbers for Cs are $n(\varepsilon_F) = 20.32$, $n_0(\varepsilon_F) = 8.85$, $n_1(\varepsilon_F) = 4.55$, $n_2(\varepsilon_F) = 6.81$ and $n_3(\varepsilon_F) = 0.17$. In the case of Na the average shape of the unoccupied part of the DOS curve is similar to a free-electron parabola. The observed structure is due to the fact that the total DOS is a superposition of rather sharply peaked contributions from the individual bands whose energy ranges overlap (the broken lines in figure 1(a)). The same statements hold for the angular-momentum-resolved partial densities of states whose smoothened energy dependence is essentially free-electron-like (figure 1(b)).

In sharp contrast to the behaviour of Na, individual bands or groups of a few bands give rise to pronounced and distinctly separated peaks in Cs: the structure between 0.2 and 0.3 Ryd is due to bands 2 and 3, whereas bands 4–6 cause the peaks in the energy range between 0.3 and 0.48 Ryd (the broken lines in figure 2(a)). These bands are predominantly of d character. Above 0.5 Ryd the f character (bands 7–20) becomes more and more important (figure 2(b)). This profound variance in the band structures of Na and Cs can be expected to cause important differences between the density fluctuation spectra of these two substances. In particular, the features of the unoccupied bands of Cs, showing rather transition-metal- than free-electron-like behaviour, may lead to strong damping of plasmon excitations for wave vector lengths well below the critical value for Landau damping resulting from continuum models.

These band structure results are in close agreement with those of, e.g., Ham (1962), Kenney (1964) and Papaconstantopoulos (1986) in the case of Na covering an energy range of 1.5 Ryd and with those of Kenney (1967), Lawrence (1971) and Papaconstantopoulos (1986) in the case of Cs extending up to 0.5 Ryd.

3. Formalism

The Bethe–Salpeter equation for the response functions in the RPA–LDA approximation may be derived by applying external fields to the Dyson equation for the one-particle band structure Green function, g, and evaluating its change, δg, to first order. In the case of the density response we consider the perturbation caused by the scalar space- and time-dependent potential $\Phi(r, t)$. The Dyson equation for g reads

$$\left(i\frac{\partial}{\partial t}\Phi(r,t) + \Delta - V(r, n(r,t))\right) g(rt, r't') = \delta(r - r')\delta(t - t') \tag{1}$$

with

$$V(r, n(r,t)) = 2\int dr' \frac{n(r',t)}{|r - r'|} + V_{xc}(n(r,t)). \tag{2}$$

In setting up equations (1) and (2) we neglect relaxation and retardation effects, that is we assume the same dependence of the effective one-particle potential, V, on the density as in

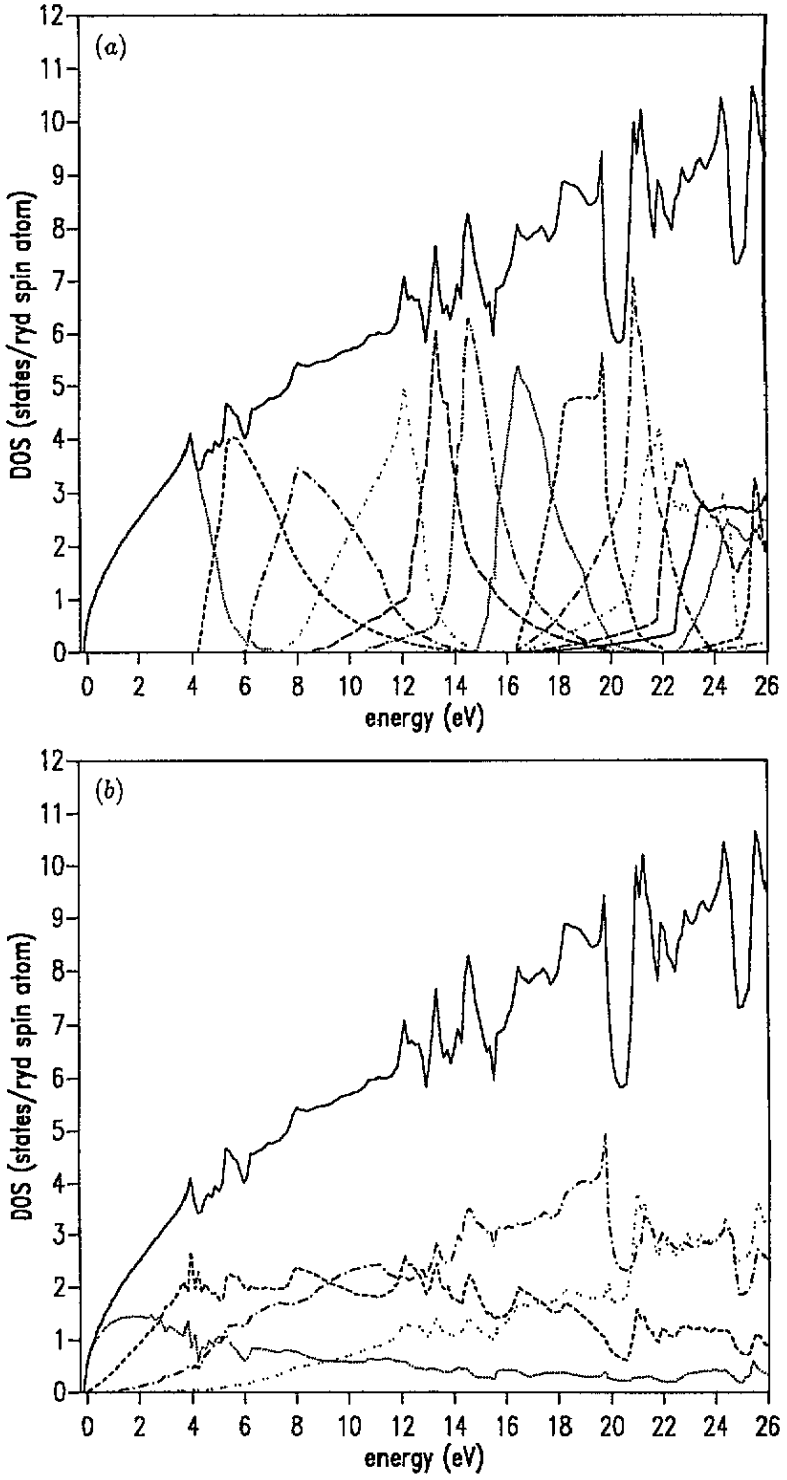

Figure 1. The density of states of Na. (*a*) The total DOS (solid line) as a sum of the contributions from the individual bands (broken lines). (*b*) Contributions of individual angular momenta to the total DOS. ·····, $l = 0$; – – –, $l = 1$; — · —, $l = 2$; ·· ··, $l = 3$.

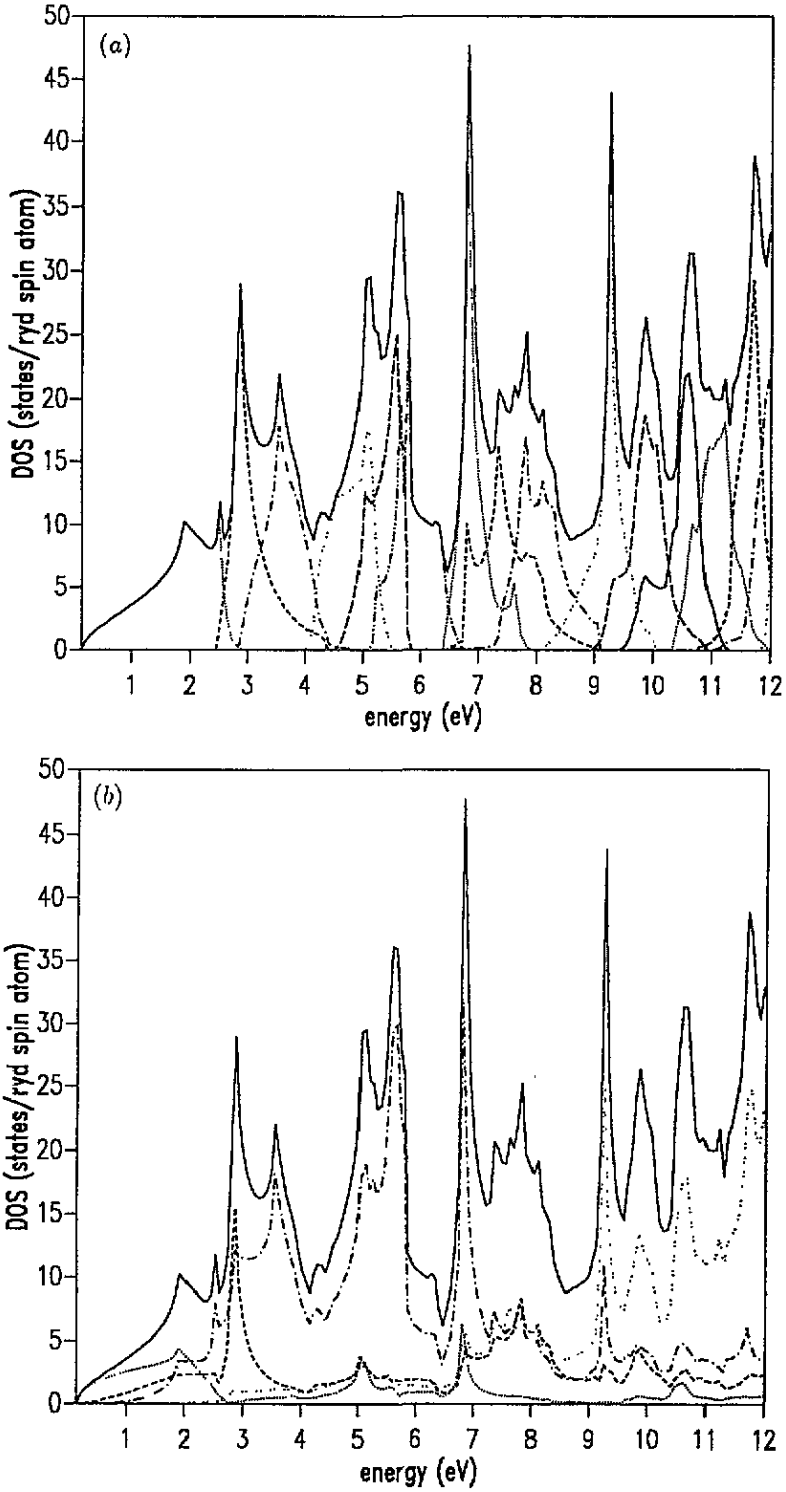

Figure 2. The density of states of Cs. (*a*) The total DOS (solid line) as a sum of the contributions from the individual bands (broken lines). (*b*) Contributions of individual angular momenta to the total DOS. ·····, $l = 0$; – – –, $l = 1$; — · —, $l = 2$; ·· ··, $l = 3$.

equilibrium. Linearizing equation (1), we obtain for the change, δg, of g

$$\delta g(rt, r't') = \int dr_1\, dt_1 g_n(rt, r_1t_1)g_n(r_1t_1, r't')\Phi(r_1, t_1) + \int dr_1\, dt_1\, dr_2 g_n(rt, r_1t_1)g_n(r_2t_1, r't')K(r_1, r_2)\delta n(r_2, t_1) \tag{3}$$

with

$$K(r_1, r_2) = \delta V(r_1)/\delta n(r_2). \tag{4}$$

The Fourier transform of the equilibrium Green function, g_n, reads in terms of the Bloch states, $\Psi_{k\lambda}$, and the energy eigenvalues $\varepsilon_{k\lambda}$

$$g_n(r, r'; \omega) = \sum_\lambda \int \frac{dk}{\Omega_{BZ}} \Psi_{k\lambda}(r) \frac{1}{\omega - \varepsilon_{k\lambda}} \Psi^*_{k\lambda}(r'). \tag{5}$$

Equation (5) involves summation over the bands λ and integration over the Brillouin zone of volume Ω_{BZ}.

Relating the density response, δn, to the perturbation, Φ, through the relation

$$\delta n(r, t) = \frac{1}{i}\delta g(rt, rt^+) = \int dr'\, dt' \chi^d(rt, r't')\Phi(r', t') \tag{6}$$

and using equation (3), we obtain the following integral equation for the Fourier transform of the density correlation function, χ^d:

$$\chi^d(r, r'; \omega) = \chi^p(r, r'; \omega) + \int dr_1\, dr_2 \chi^p(r, r_1; \omega)K(r_1, r_2)\chi^d(r_2, r'; \omega). \tag{7}$$

In our applications we work with the lattice Fourier transforms of the space-dependent quantities. In this representation the non-interacting susceptibility, χ^p, reads in terms of the one-particle Green function

$$\chi^p_q(\rho\tau, \rho'\tau'; \omega) = \frac{2}{\pi} \int d\varepsilon \int \frac{dk}{\Omega_{BZ}} (f(\varepsilon)\,\mathrm{Im}\, g^{ret}_{k+q}(\rho\tau, \rho'\tau'; \varepsilon)g^{ret}_k(\rho'\tau', \rho\tau; \varepsilon + \omega) + f(\varepsilon + \omega)g^{av}_{k+q}(\rho\tau, \rho'\tau'; \varepsilon)\,\mathrm{Im}\, g^{ret}_k(\rho'\tau, \rho\tau; \varepsilon + \omega)). \tag{8}$$

Here, ρ and ρ' are local coordinates in the vicinities of sites τ and τ' and the wave vectors q are restricted to the first BZ. The following form of the lattice Fourier transform of the **K** matrix has been derived by Winter (1993):

$$K_q(\rho\tau, \rho'\tau') = \sum_{lml'm'} Y_{lm}(\rho)Y_{l'm'}(\rho')(K^{C,1}_{lm,l'm'}(\rho\tau, \rho'\tau') + K^{C,2}_{lm,l'm'}(\rho\tau, \rho'\tau')) + K_{xc}(\rho, \tau)\delta(\rho - \rho')\delta_{\tau\tau'} \tag{9}$$

with

$$K^{C,1}_{lm,l'm'}(\rho\tau, \rho'\tau') = \rho^l \rho'^{l'} B^{\tau\tau'}_{lm,l'm'}(q)$$

and

$$K^{C,2}_{lm,l'm'}(\rho\tau, \rho'\tau') = [8\pi/(2l+1)]((\rho^l/\rho'^{l+1})\Theta(\rho'-\rho) + (\rho'^l/\rho^{l+1})\Theta(\rho-\rho'))\delta_{\tau\tau'}\delta_{ll'}\delta_{mm'}.$$

The site off-diagonal part, $K^{C,1}$, of the Coulomb interaction, which is proportional to $1/q^2$ for small wave vectors, is separable with respect to its space arguments. This is not the case for the on-site Coulomb term $K^{C,2}$ and the local expression for the exchange and correlation part K_{xc}. Corrections to formula (9) existing in regions with

$$|\rho + \rho'| > |R + \tau - \tau'|$$

(R is any lattice vector) lead to errors in the Fourier transform of K^C below 1% and can safely be neglected.

The form of $\mathbf{K}$ displayed in equation (9) suggests dividing the problem of solving the Bethe–Salpeter equation for χ^d into two steps. We introduce the auxiliary function $\tilde{\chi}$ through the following equation:

$$\tilde{\chi}_q(\rho\tau, \rho'\tau') = \chi^p_q(\rho\tau, \rho'\tau'; \omega) + \sum_{\tau_1\tau_2}\int d\rho_1\, d\rho_2\, \chi^p_q(\rho\tau, \rho_1\tau_1; \omega)K^{C,1}(\rho_1\tau_1, \rho_2\tau_2)\tilde{\chi}_q(\rho_2\tau_2, \rho'\tau'; \omega). \quad (10)$$

Equation (10) can be solved for $\tilde{\chi}$ exploiting the separability of its kernel. The geometry of the interstitial region is thereby rigorously taken into account. More details, concerning this point, are given in the appendix. To evaluate χ^d the following equation remains to be solved:

$$\chi^d_q(\rho\tau, \rho'\tau') = \tilde{\chi}_q(\rho\tau, \rho'\tau'; \omega) + \sum_{\tau_1}\int d\rho_1\, \tilde{\chi}_q(\rho\tau, \rho_1\tau_1; \omega)K^{nsep}(\rho_1\tau_1)\chi^d_q(\rho_1\tau_1, \rho'\tau'; \omega). \quad (11)$$

In equation (11) we introduced the symbol K^{nsep} for the sum of the on-site Coulomb and the exchange–correlation term. Equation (11) may be solved for χ^d by expanding the radial parts of the single-site one-electron wave functions with respect to energy as described in previous work (Stenzel and Winter 1986). Second-order expansions proved sufficient in the present application.

The real space double Fourier transforms discussed in the following sections are defined in terms of the lattice Fourier transforms in the following way:

$$\chi(q, q; \omega) = \sum_{\tau_1,\tau_2}\int d\rho_1\, d\rho_2\, \exp(iq(\rho_2 + \tau_2 - \rho_1 - \tau_1))\chi_q(\rho_1\tau_1, \rho_2\tau_2; \omega). \quad (12)$$

Instead of the correlation functions, χ, the quantities commonly considered in the literature are the dielectric functions ε and ε^{-1}. They are related to the χ functions through the following relations:

$$\varepsilon(q, q; \omega) = 1 - (8\pi/q^2\Omega_{unit})\chi^p(q, q; \omega) \quad (13)$$

and

$$\varepsilon^{-1}(q, q; \omega) = 1 + (8\pi/q^2\Omega_{unit})\chi(q, q; \omega). \quad (14)$$

Only in the case of a translationally invariant system is ε^{-1} the inverse of ε. In the following we present and discuss results for the dielectric functions.

4. The dielectric functions

We employed our band structure results to construct the one-particle Green function using equations (5) and (8) and to evaluate the lattice Fourier transform of the dielectric function ε as a function of frequency and the local real space coordinates for some wave vectors in the (1,0,0) direction. The way the BZ integrations hereby involved, including the k- and space-coordinate-dependent matrix element vectors, are handled has been described in previous papers (Stenzel and Winter 1986, Götz and Winter 1993). For convenience we discuss the features of ε by considering the real and the imaginary part of its real space Fourier transform $\varepsilon(q, q; \omega)$, as defined in equation (13).

In figure 3 we show both the real and the imaginary part of the dielectric function of Na in its dependence on frequency for different wave vectors q. According to equations (5) and (8) it consists of the sum of matrix-element-weighted transitions between the occupied part of band 1 and the unoccupied part of band 1 (intraband contributions) on the one hand and the unoccupied bands (interband contributions) on the other. Also drawn are the individual contributions to $\mathrm{Im}\,\varepsilon$ from transitions between bands 1 and n ($1 \leqslant n \leqslant 6$) and the sum of transitions from band 1 to bands 7–19. To emphasize their importance for the density fluctuation spectra some of them are multiplied by the factor $1/q^2$ (those with $n \geqslant 2$ in the case of $q = 0.1$ and those with $n > 2$ in the cases $q = 0.2$ and $q = 0.3$ (du)). This factor compensates for the smallness of the involved interband matrix elements squared, being roughly proportional to q^2 at long wavelengths. Whereas for $q < 0.1$ (du) the intraband contribution is separated from the others by a small gap, it spreads out on increasing wave vectors, overlapping the energy ranges of an increasing number of interband transitions. It thereby loses height and its initial slope decreases. This leads to a decrease of the wave-vector-dependent static dielectric function. In agreement with the features of the DOS curve the individual interband contributions are sharply structured and in sequence of their energetic positions their amplitudes increase. This can lead to pronounced peaks in the total dielectric function as a glance at the curve for $q = 0.6$ (du) shows, where the transitions between bands 1 and 4 cause the spiky structure around 7.4 eV. This behaviour of the imaginary part is reflected in the Kramers–Kronig-related real part of $\varepsilon(q, q; \omega)$. Whilst for small wave vectors it looks quite free-electron-like, important deviations from the free-electron shape become visible for q values > 0.3 (du), especially in the frequency range between 6 and 8 eV, where the plasmon-like excitations of the density fluctuation spectrum are expected to show up.

The corresponding curves for Cs are displayed in figure 4. In this case the intraband contribution is very different from the free-electron picture even at small wave vectors. It is appreciably structured and shows a sharp band edge peak. This behaviour can be traced back to the fact that the Fermi level falls outside the parabolic part of the first band. For $q < 0.15$ (du) the contribution due to transitions between bands 1 and 2 is separated from the intraband contribution by a distinct gap. On increasing q the broadening of the intraband term leads to a merging of these two structures. Most striking is the high amplitude of this interband peak, which is caused by the nearness of important parts of the Fermi surface to the BZ boundary, where, due to their energetic vicinity, a mixing of characters between bands 1 and 2 occurs. The transitions to the higher bands lead to the individual peaks (partly multiplied by factors $1/q^2$ in the figures) in full compatibility with the properties of the DOS curve. They cause modulations in the shape of the dielectric function for frequencies above 2 eV with important consequences for the RPA density fluctuation spectrum. Especially remarkable in this connection is the dip in the vicinity of $\omega = 4.8$ eV, caused by the separation between the complex consisting of bands 1–6 on one side and the higher bands

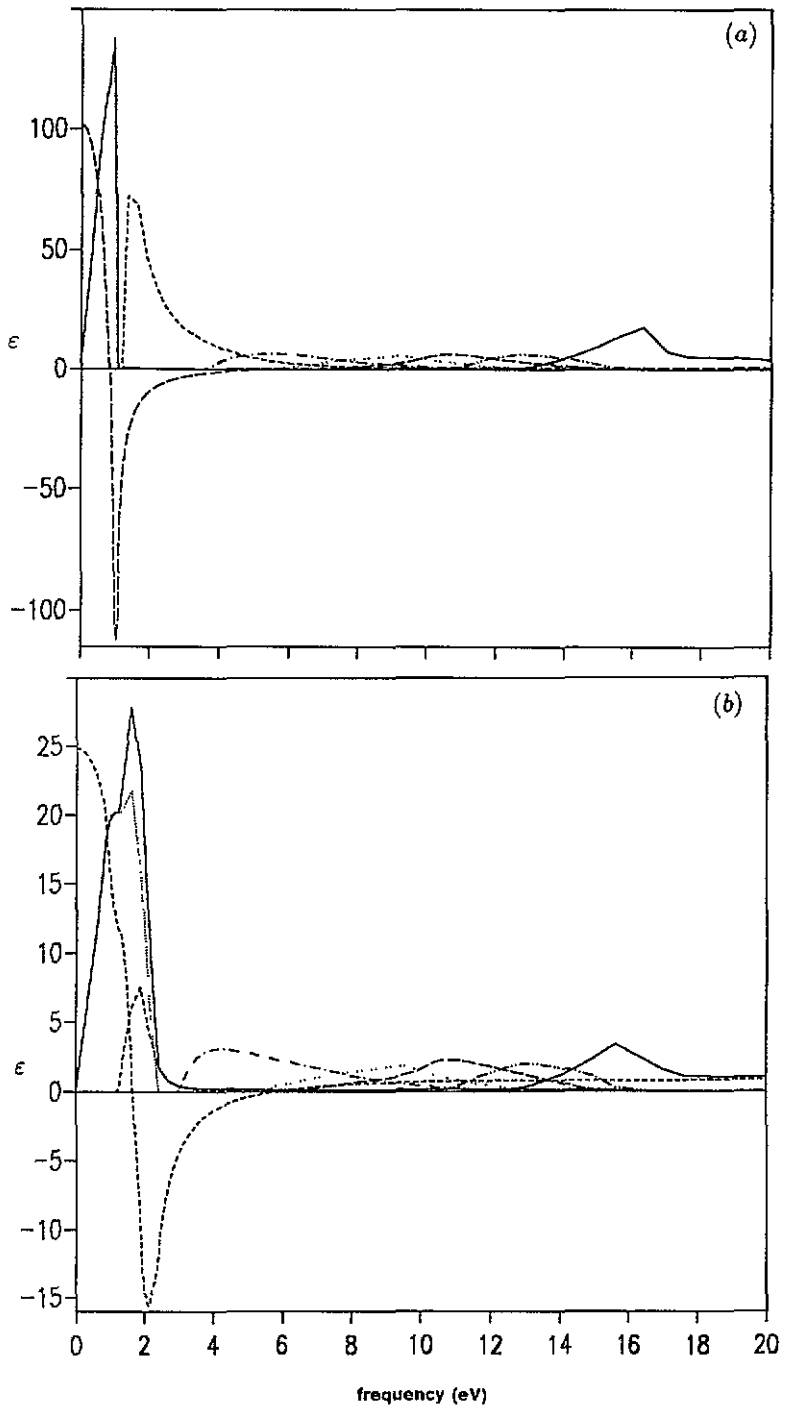

Figure 3. The dielectric function, $\varepsilon(q, q; \omega)$, of Na for q in the (1,0,0) direction. The values of q are in units of $2\pi/a$ (du). Real part: — — —. Imaginary part: total: ——, individual contributions: ·····, transitions from band 1 to band 1; - - - -, to band 2; — · —, to band 3; ·· ··, to band 4; — — —, to band 5; — · · —, to band 6; ——, to bands 7–12. (*a*) $q = 0.1$, (*b*) $q = 0.2$, (*c*) $q = 0.4$, (*d*) $q = 0.5$, (*e*) $q = 0.6$. Those partial contributions in the drawings with amplitudes larger than the total imaginary part of ε are multiplied by factors of $1/q^2$.

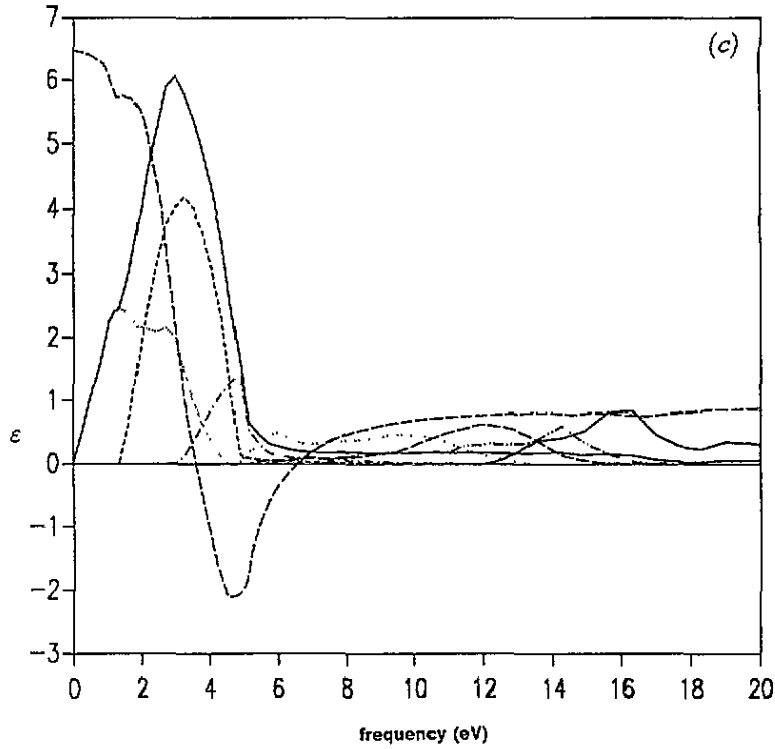

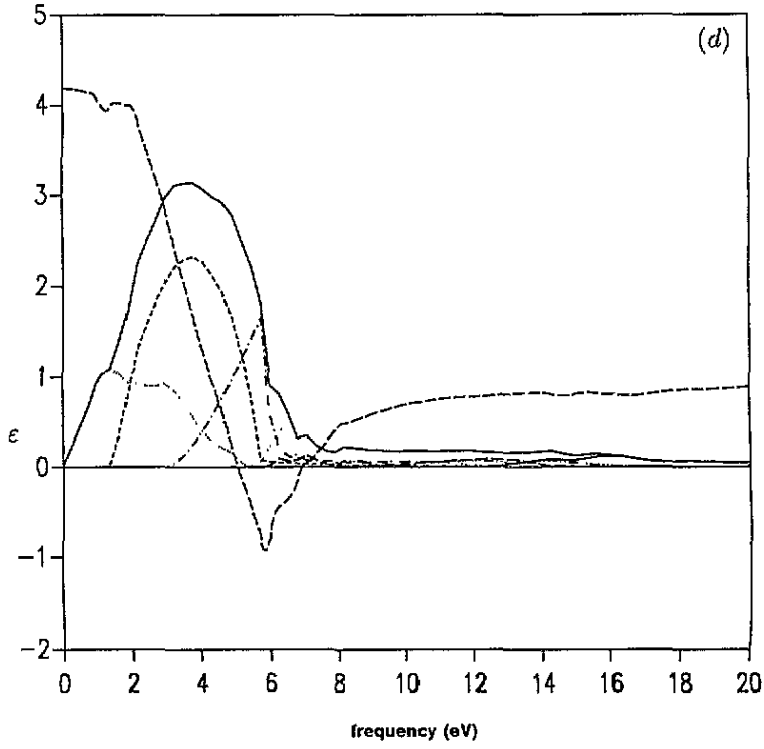

Figure 3. (Continued)

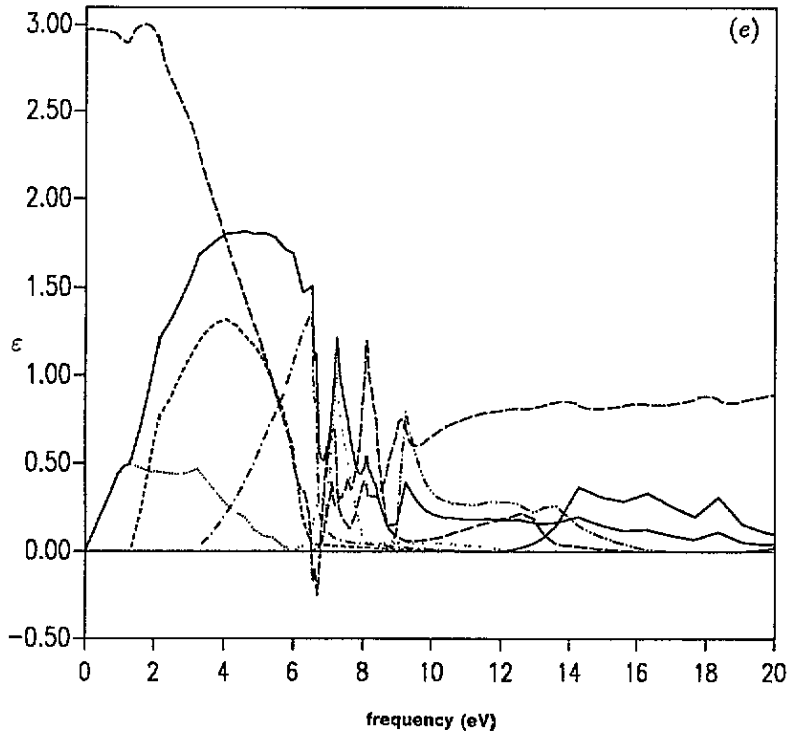

Figure 3. (Continued)

on the other side. The curves for the real part of the dielectric function once again underline that Cs deviates substantially from the free-electron behaviour.

5. The density fluctuation spectra

We used the program sketched in section 3 to evaluate $\varepsilon^{-1}(q, q; \omega)$ for the wave vector values $q = 0.1$, 0.2, 0.3, 0.4, 0.5 and 0.6 (du) in the case of Na and for the numbers $q = 0.1$, 0.2, 0.3 and 0.6 (du) in the case of Cs. The q vectors pointed in the (1,0,0) direction. Other, less symmetric directions would not cause any additional problems, except for a moderate increase in CPU time, which, however, is irrelevant, because we optimized our codes to run them on an IBM-risc workstation.

The evaluation of density fluctuation spectra demands a higher degree of accuracy at high frequencies than the otherwise similar problem of treating spin fluctuations. Since the Coulomb interaction is repulsive and diverges as $1/q^2$ at small wave vectors, large amplitudes of $\operatorname{Im}\varepsilon^{-1}$ are found roughly at positions ω_p fulfilling the condition

$$\operatorname{Re}\varepsilon(q, q; \omega_p) = \operatorname{Re}(1 - (8\pi/\Omega_{unit}q^2)\chi^p(q, q; \omega)) = 0$$

provided $\operatorname{Im}\chi^p(q, q; \omega_p)$ is not too big. These frequencies lie in general well above the main peaks of χ^p. Especially at small wave vectors, $\operatorname{Im}\chi^p(q, q; \omega_p)$ is determined by interband transitions giving rise to amplitudes proportional to q^2. The corresponding calculations therefore require special care including the treatment of interstitial regions. On the other

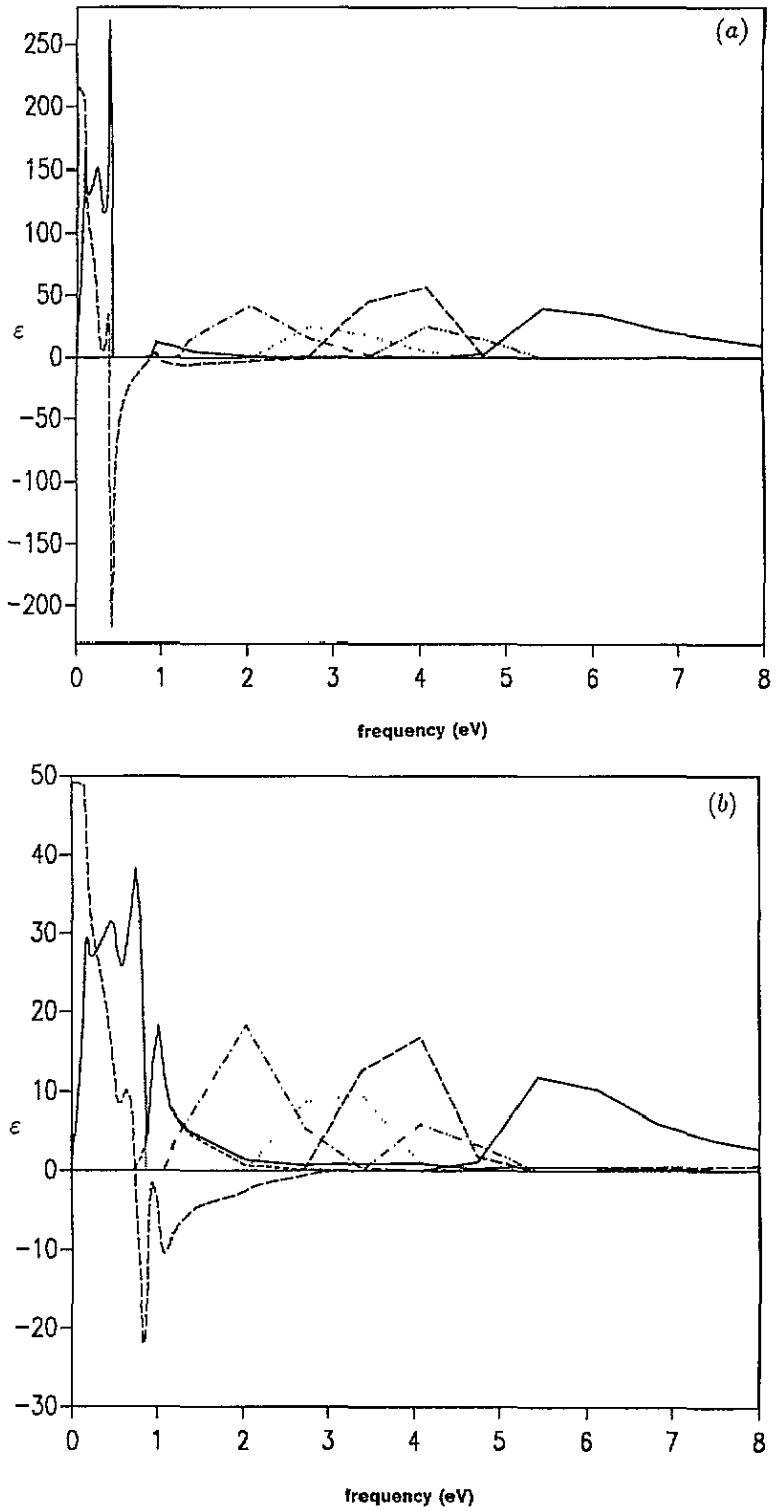

Figure 4. The dielectric function, $\varepsilon(q, q; \omega)$ of Cs. The meanings of the curves are the same as in the case of figure 3. (*a*) $q = 0.1$, (*b*) $q = 0.2$, (*c*) $q = 0.3$, (*d*) $q = 0.6$ (du).

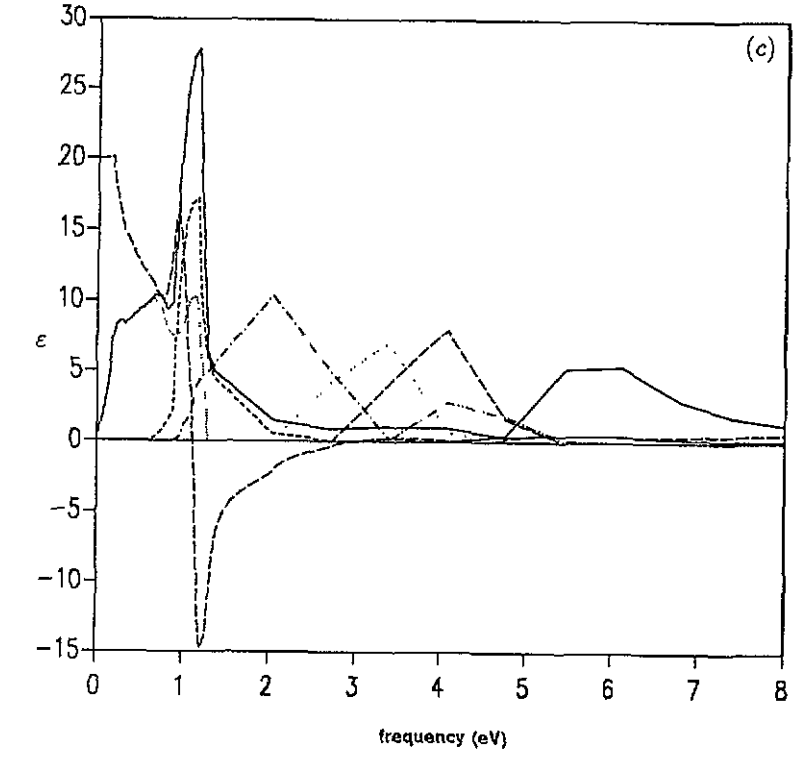

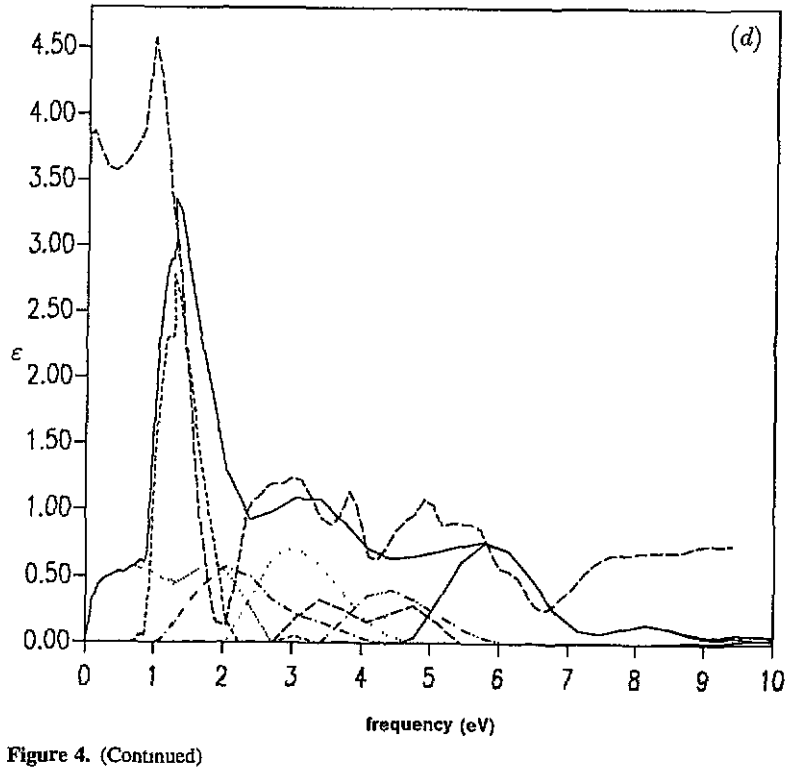

Figure 4. (Continued)

hand, rapid variations with frequency are a genuine property of RPA dielectric functions, especially at energies near thresholds for transitions between particular pairs of bands, and are not caused by any kind of improper handling of the numerical problem. They may give rise to rather noisy structures in the RPA density fluctuation spectrum, which would probably be wiped out by any augmentation of the RPA. Only the gross features obtained within this approximation should therefore be taken seriously.

Within a finite-wave-vector regime we find clear-cut plasmon-like excitations in Na, as figure 5 demonstrates. An appreciable amount of damping is, however, already present at small wave vectors. It is caused by the significance of umklapp scattering as a consequence of the lattice structure. This is remarkable in view of the fact that Na resembles a free-electron system in some aspects. The dispersion of these plasmons has a positive fourth-order term becoming perceptible for q values above 0.4 (du). The lifetime of the plasmons diminishes appreciably with increasing wave vector and, slightly above the critical value for Landau damping in a homogeneous electron gas ($q_c \simeq 0.5$ (du)), they dissolve into broad structures. The subpeaks in the curve for $q = 0.6$ (du) can be clearly traced back to features in the band structure (figure 1) and consequently in the spiky shape of the polarization function (figure 3) due to the interband transitions 1–4 and 1–5. The values for the theoretical positions and widths of the plasmons are displayed in table 1. The values of table 1 extrapolate to $\omega_p = 5.68$ eV and $\Gamma = 0.41$ eV for $q \to 0$. These numbers are very near to the experimental results $\omega_p = 5.72$ eV (Kunz 1966) and 5.70 eV (Sueoka 1965, Kloos 1973). These authors observe a plasmon line width of 0.4 eV, also in good agreement with our findings. Our plasmon dispersion curve compares favourably to the measurements of vom Felde and coworkers (1989) with maximum deviations of 1.5%.

In agreement with our findings Aryasetiawan and Karlsson (1994) obtain clear-cut plasmon peaks in their theoretical work. Their plasmon frequencies, starting at about 6 eV in the long-wavelength limit and rising to about 7.7 eV at $q = 0.5$ du, are somewhat above our values. The RPA calculations of Quong and Eguiluz (1993) for Na also yield plasmon excitations with energies at 6 eV for $q = 0$ and 7.9 eV at $q = 0.5$ du. Their TDLDA values for finite wave vectors are slightly lower ($\omega_p = 7.4$ eV for $q = 0.5$ du).

As can be expected from the band structure results and the characteristics of the dielectric function ε, the RPA–LDA loss function $\mathrm{Im}\,\varepsilon^{-1}(q, q; \omega)$ of Cs is not as simple as that of Na. In Cs the 5p core levels are only about 0.6 Ryd below the bottom of the valence band and may thus influence the density fluctuation spectrum appreciably even in the energy range of a few electronvolts. We therefore included the 5p core levels in our numerical evaluation of ε^{-1} on the same footing as the valence bands and show the results of these calculations in figure 6. Superimposed on a broad structure extending over the frequency range between 1 and 8 eV are distinct low-frequency peaks. Their positions ω_p vary from about 3.0 eV at $q = 0.1$ du to $\omega_p = 2.8$ eV at $q = 0.3$ du. At $q = 0.6$ du the peak position has again reached the small-wave-vector value. Also striking is the existence of a second peak near 4.8 eV, which is rather pronounced at small wave vectors and levels off with increasing q, shifting to slightly smaller frequencies. At $q = 0.6$ du it is hardly visible any longer. As already indicated in the preceding section, it owes its existence to variations of the polarization function in this energy region between the upper edge of contributions due to transitions between band 1 and the band complex 1–6 on one side and the lower edge of contributions due to transitions between band 1 and bands 7–12 on the other side. It is interesting to remark that the band structure calculations of Papaconstantopoulos (1986) yield a dip in the DOS curve at the same energy position as ours do. The widths (full width at half height) increase continuously with increasing q, their values Γ being 0.8 eV at $q = 0.1$ du, 1.05 eV at $q = 0.3$ du and 1.4 eV at $q = 0.6$ du. In view of the shapes

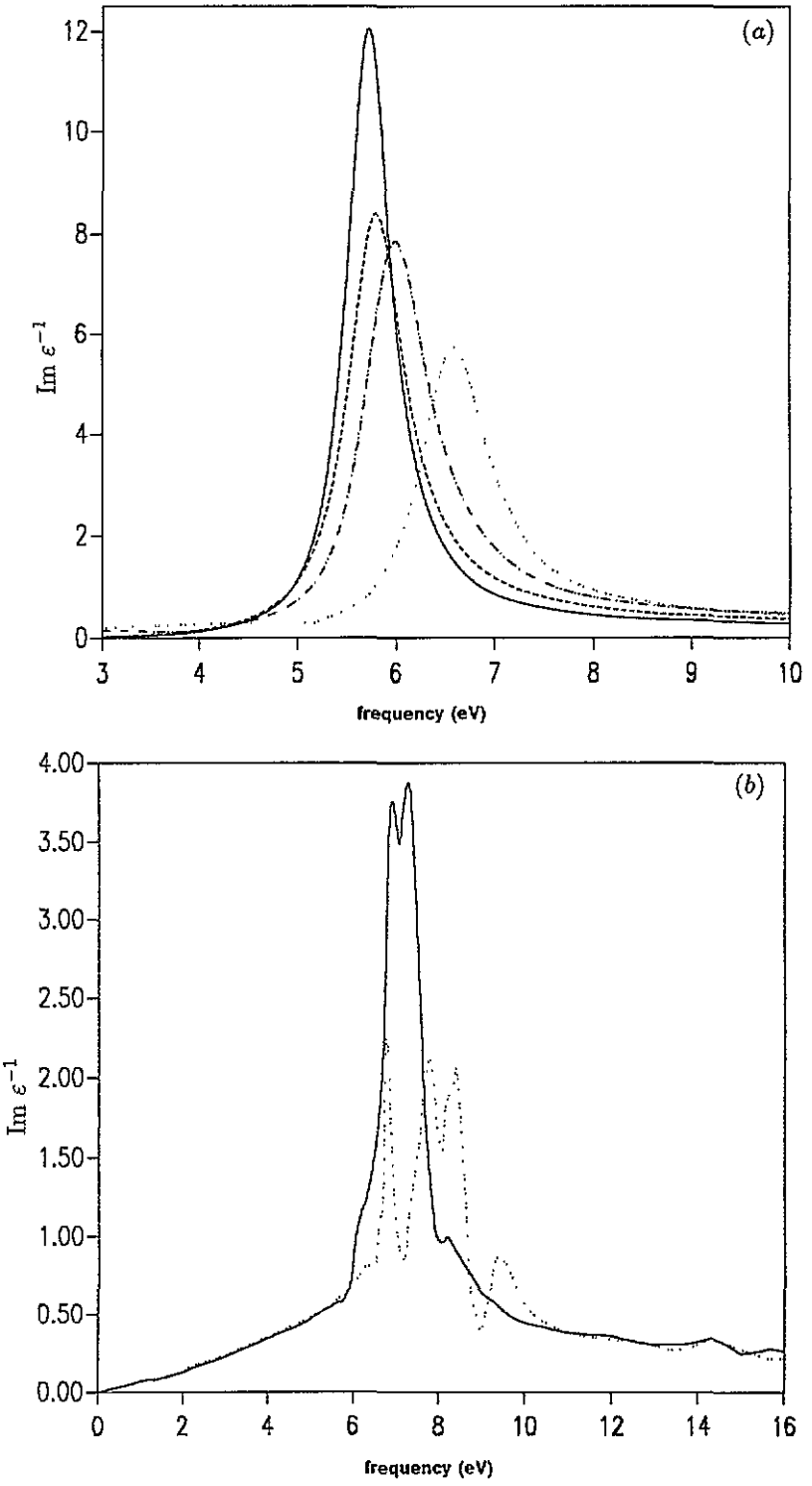

Figure 5. The imaginary part, $\mathrm{Im}\,\varepsilon^{-1}(q, q; \omega)$, of the RPA–LDA density response of Na for some q values in the (1,0,0) direction. (*a*) ——, $q = 0.1$, – – –, $q = 0.2$, — · · —, $q = 0.3$, · · ·, $q = 0.4$, (*b*) ——, $q = 0.5$, · · ·, $q = 0.6$.

of the curves it seems, however, somewhat problematic to define widths of plasmons. For comparison we also performed calculations disregarding the 5p core levels. In this case the height of the low-frequency peak is diminished in favour of the peak near 5 eV and the amplitudes of the fluctuation spectrum between the peaks are increased. These observations clearly demonstrate the importance of the 5p core levels for the density response.

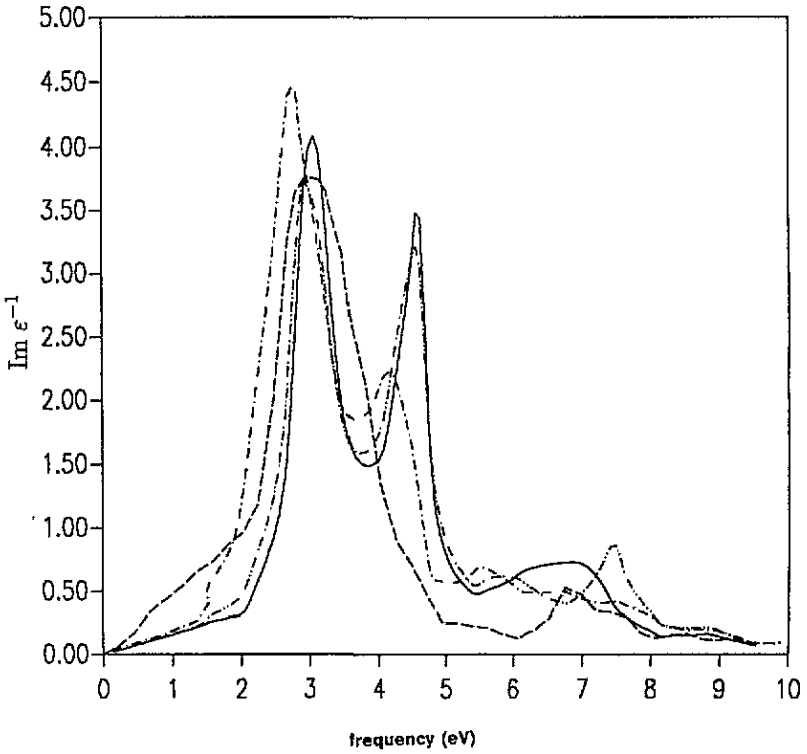

Figure 6. The imaginary part, $\varepsilon^{-1}(q, q; \omega)$ of the RPA–LDA density response of Cs for some q values in the (1,0,0) direction. ——, $q = 0.1$, — · · —, $q = 0.2$, — · —, $q = 0.3$, – – –, $q = 0.6$.

Table 1. Positions and widths of plasmon excitations in Na.

Wave vector q (du)	Peak position ω_p (eV)	Width (FWHH) Γ (eV)
0.1	5.71	0.54
0.2	5.81	0.73
0.3	5.985	0.84
0.4	6.59	0.89
0.5	7.04	1.05

Our results may be compared to the EELS experiments of Kunz (1966), who measured ε^{-1} of Cs for zero momentum transfer, obtaining $\omega_p = 2.9$ eV and $\Gamma = 1.2$ eV. His value for

ω_p compares favourably with the position of our low-frequency peak at small wave vectors, whereas his Γ value is somewhat above ours. Vom Felde *et al* (1987) report on q-dependent EELS measurements for Cs, observing strongly damped plasmons within an extended wave vector region. The plasmon dispersion derived from their experiments exhibits negative dispersion in the wave vector range $0 < q < 0.48$ du. Their long-wavelength value of ω_p is 2.9 eV and the minimum at $q = 0.48$ du is 2.72 eV. For Γ they find 0.8 eV at small q rising linearly to $\Gamma = 1.2$ eV at $q = 0.6$ du. Our low-frequency peak shows qualitatively similar features. Its position for $q = 0.3$ du lies distinctly below that at $q = 0.1$ du. At variance with the experiment, however, it has already reached the long-wavelength value near $q = 0.6$ du. Our Γ values are reasonably near to those of the experiment.

The theoretical results of Aryasetiawan and Karlsson (1994), based on LMTO band structure and performed for wave vectors in the (1,1,0) direction, show plasmon peaks at positions some tenths of an electronvolt above ours. With increasing q they exhibit broad shoulders. Additional small peaks appear near 6 eV. The peak near 4.8 eV at small wave vectors resulting from our calculations does not show up in theirs. In agreement with experiment they obtain negative dispersion in a certain wave vector range. Thus there are similarities and differences between their results and ours. If, however, one takes into account that different band structure methods underlie these two independent treatments and that relatively minor variances in the energy bands, in the characters of the Bloch states and in details of the calculations may lead to important changes in the density fluctuation spectra, the differences between the results do not seem too serious to us.

6. Summary

We applied our first-principles approach, developed for evaluating correlation functions, to the density response of alkali metals. Since we work in the local angular momentum representation, the lattice structure is rigorously taken into account, avoiding any truncation in reciprocal lattice space. This method is generally applicable to the whole spectrum of substances ranging from simple metals to narrow-band transition metals. As a consequence of the strength and the repulsive character of the Coulomb interaction, the involved numerics require an especially high degree of accuracy. The interesting features of the density fluctuation spectra appear at frequencies well above the large-amplitude regimes of the polarization functions. To calculate the latter reliably, we need to know the one-particle Green functions in real space, including the interstitial regions and within an extended energy range. The band structure method used should ensure the fulfilment of the f sum rule, as is the case with the KKR. Our calculated KKR data for Na and Cs lead to tolerable deviations from this sum rule, decreasing with increasing wave vector. Altogether we feel that our results for the density response are trustworthy from a numerical point of view and the discussions of the previous sections show that they are interpretable in terms of band structure properties. We have demonstrated that the step to implement the theory with the lattice structure leads to a significant improvement of RPA-based results over continuum models. Our results for Cs show that it is dangerous to consider the alkali metals as nearly-free-electron systems when dealing with density correlations, since the properties of unoccupied bands may substantially deviate from this behaviour. The light alkali metals on the other hand seem to be nearer to this picture and, as our results for Na suggest, RPA LDA yields values for the positions and widths of their plasmonic excitations in satisfying agreement with experiment. In the case of Cs our calculations reproduce important features of the experiment. In significant points they are also in accordance with other theoretical

work discussed in the present paper. Remaining differences may be caused by the use of different band structure methods and variances in computational details such as the way the BZ integrals are performed. They clearly point out the difficulties involved in these kinds of calculation. The formalism presented is flexible enough for treating improvements of the **K** matrix and the one-particle Green function beyond the RPA and this should be the aim of future applications.

Appendix

To solve equation (10) for $\tilde{\chi}$ we insert the expression for $K^{C,1}$ (equation (9)) into equation (10), obtaining

$$\tilde{\chi}_q(\rho\tau, \rho'\tau'; \omega) = \chi_q^p(\rho\tau, \rho'\tau'; \omega) + \sum_{l_1m_1\tau_1, l_2m_2\tau_2} \chi_q^p(\rho\tau|l_1m_1\tau_1) B^{\tau_1\tau_2}_{l_1m_1, l_2m_2}(q) \tilde{\chi}(l_2m_2\tau_2|\rho'\tau') \tag{A1}$$

with

$$\chi_q^p(\rho\tau|l_1m_1\tau_1; \omega) = \int_{(\tau_1)} \mathrm{d}\rho_1 \, Y_{l_1m_1}(\rho_1)\rho^{l_1} \chi_q^p(\rho\tau, \rho_1\tau_1; \omega) \tag{A2}$$

and

$$\tilde{\chi}_q(l_2m_2\tau_2|\rho'\tau'; \omega) = \int_{(\tau_2)} \mathrm{d}\rho_2 \, Y_{l_2m_2}(\rho_2)\rho^{l_2} \tilde{\chi}_q(\rho_2\tau_2, \rho'\tau', \omega). \tag{A3}$$

The equation for $\tilde{\chi}_q(lm\tau|\rho'\tau'; \omega)$ may easily be derived from equation (A1). We obtain

$$\tilde{\chi}_q(lm\tau|\rho'\tau'; \omega) = \chi_q^p(lm\tau|\rho'\tau'; \omega) + \sum_{l_1m_1\tau_1, l_2m_2\tau_2} \chi_q^p(lm\tau|l_1m_1\tau_1; \omega) B^{\tau_1\tau_2}_{l_1m_1, l_2m_2}(q) \tilde{\chi}(l_2m_2\tau_2|\rho'\tau'; \omega) \tag{A4}$$

with

$$\chi_q^p(lm\tau|l_1m_1\tau_1; \omega) = \int_{(\tau)} \mathrm{d}\rho \, Y_{lm}(\rho)\rho^l \chi_q^p(\rho\tau|l_1m_1\tau_1; \omega). \tag{A5}$$

Lumping the quantum numbers $(lm\tau)$ into one-dimensional index fields, equation (A4) can be solved for $\tilde{\chi}_q(lm\tau|\rho'\tau'; \omega)$ by matrix inversion. The spatial integrals in equations (A1)–(A5) are over the Wigner–Seitz cells of the corresponding sites, allowing for rigorous integrations over the interstitial regions. Inserting $\tilde{\chi}_q(lm\tau|\rho'\tau'; \omega)$ into equation (A1), we obtain $\tilde{\chi}_q(\rho\tau, \rho'\tau'; \omega)$ in full dependence on its space coordinates.

References

Aryasetiawan F and Karlsson K 1994 *Phys. Rev. Lett.* **73** 1679
Götz W and Winter H 1993 *J. Phys.: Condens. Matter* **5** 1707
Ham F S 1962 *Phys. Rev.* **128** 82
Ham F S and Segall B 1961 *Phys. Rev.* **124** 1786
Hedin L and Lundqvist B 1971 *J. Phys. C: Solid State Phys.* **4** 2064
Kenney J Q 1964 *Prog. Rep. Solid State Mol. Theor. Group, MIT* **53** 38
—— 1967 *Prog. Rep. Solid State Mol. Theor. Group, MIT* **66** 3
Kloos T 1973 *Z. Phys.* **265** 225
Kollwitz M and Winter H 1994 *Verhandlungen der Deutschen Physikalischen Gesellschaft 5, 1994 Spring Meeting* (Mostbach: Physik) p 1299
Kunz C 1966 *Z. Phys.* **196** 311
Lawrence M J 1971 *J. Phys. F: Met. Phys.* **1** 836
Papaconstantopoulos D A 1986 *Handbook of the Bandstructure of Elemental Solids* (New York: Plenum)
Quong A A and Eguiluz A G 1993 *Phys. Rev. Lett.* **70** 3955
Stenzel E and Winter H 1986 *J. Phys. F: Met. Phys.* **16** 1789
Sueoka O 1965 *J. Phys. Soc. Japan* **20** 2203
vom Felde A, Fink J, Büche Th, Scheerer B and Nücker N 1987 *Europhys. Lett.* **4** 1037
vom Felde A, Sprösser-Prou J and Fink J 1989 *Phys. Rev.* B **40** 10 181
Winter H 1993 *Z. Phys.* B **91** 343
Zaremba E and Sturm K 1991 *Phys. Rev. Lett.* **66** 2144